Optical photothermal infrared imaging of fatty acid esterification in the ER of living cells

Hannah B. Castillo, Caitlin M. Davis*

Department of Chemistry, Yale University, New Haven, Connecticut, 06511, USA.

E-mail: c.davis@yale.edu

Abstract

Lipotoxicity is an accumulation of lipids that leads to cell death and metabolic disease. Saturated fatty acids are more likely to cause lipotoxicity, however, the mechanism remains unclear due to challenges visualizing reactions in live cells. Here, we use optical photothermal infrared (OPTIR) microspectroscopy to investigate palmitic acid (PA) metabolism in hepatocytes with sub-micron spatial resolution. Upon PA feeding, we discover a time-dependent ester carbonyl stretch localized to the ER near lipid droplets with abnormal morphology. This stretch is assigned to diacylglycerol intermediates in the glycerol-3-phosphate pathway. C-D stretches of deuterated PA provide complementary molecular details, supporting a model whereby PA acyl chain packing in the ER reduces enzyme diffusion slowing PA metabolism. Our results provide a deeper understanding of how phase changes induced by high melting temperature fatty acids and their metabolites change ER chemistry as well as provides a tool for detecting chemical and environmental changes associated with lipotoxicity in live cells.

Teaser

Sub-micron IR imaging of palmitic acid metabolism in live cells reveals diacylglycerol buildup and gel phase changes in the ER.

MAIN TEXT

Introduction

Metabolic diseases such as obesity, diabetes, and metabolic dysfunction-associated steatotic liver disease (MASLD), formerly known as non-alcoholic fatty liver disease, are a major health crisis (*1*). These conditions are widespread; with a worldwide prevalence over 30%, MASLD is the most common chronic liver disease (*2*). In these diseases, lipid-induced toxicity, also known as lipotoxicity, plays a major role in their onset and development (*1*). Excess lipid accumulation in the liver, termed steatosis, can lead to even more severe conditions, such as cirrhosis and liver cancer (*1*). A key cause of steatosis is fatty acid overload, when free fatty acid (FFA) influx and synthesis exceeds the liver's ability to use FFAs as energy or store them in the form of triacylglycerols (TAGs) (*1*, *3*). While FFAs and their metabolites are essential for intracellular signaling and energy homeostasis, an overload of lipids can result in oxidative stress and cell death (*3*). Although these cell stress responses are well documented, due to difficulties directly visualizing metabolic species, the sub-cellular organization and molecular level details of the underlying chemical conversions that contribute to lipotoxicity are not well understood.

Lipid droplets (LDs) protect against lipotoxicity, serving as depots for neutral lipids. Ubiquitous in cells, LDs are composed of a core of neutral lipids bound by a phospholipid monolayer (*4*, *5*). Once regarded simply as storage pools of lipids, recent work has shown that LDs are dynamic organelle that regulate the flux of lipids through periods of growth and consumption (*4*). This process closely reflects the metabolic state of the cell, as the LD will sequester potentially toxic lipids in periods of fatty acid overload and release them when the cell is in need of energy (*5*). LDs are closely associated with the endoplasmic reticulum (ER), where the majority of hepatic TAGs are synthesized via the glycerol-3-phosphate (G3P) pathway (**Fig. 1**) (*4*, *6*). Precursors to this pathway include both exogenous fatty acids (FAs) taken up by the cell through diffusion or fatty acid transporter proteins (FATP) as well as *de novo* lipogenesis (DNL) derived FAs. Once in the cell, FAs must be activated by conjugation to coenzyme A (CoA) via long-chain acyl-CoA synthetases (ACSL), forming fatty acyl-CoA molecules (*6*). These molecules then undergo stepwise esterification to G3P by multiple enzymes in the ER membrane, ultimately forming TAGs (*7*–*9*). TAGs are deposited within the leaflets of the ER bilayer until they reach a critical concentration, resulting in phase separation and coalescing into a lipid lens that expands and eventually buds from the ER membrane in the form of a lipid droplet (*4*, *5*, *10*). While LDs serve as an excellent defense against lipotoxicity, increased levels of exogenous FAs can still lead to steatosis and have been shown to alter this carefully regulated pathway (*11*).

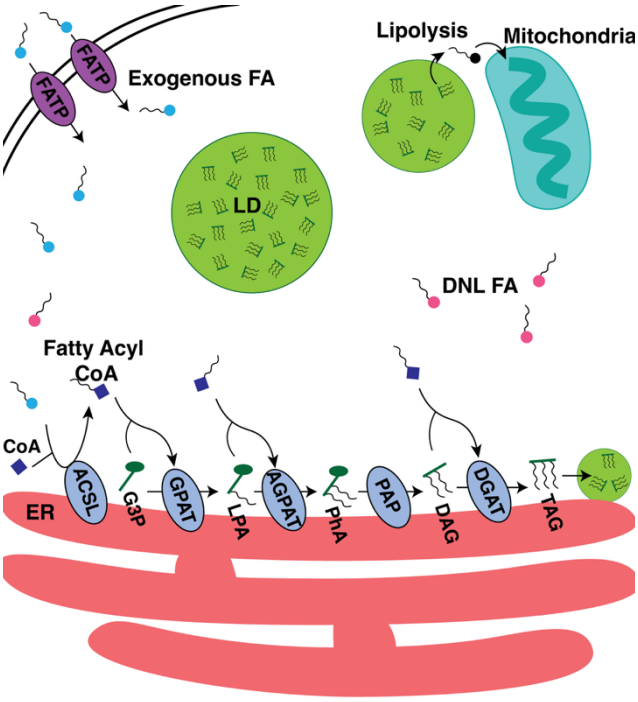

Fig. 1. Schematic of triacylglycerol synthesis via the G3P pathway. FATP, fatty acid transporter protein; ACSL, Acyl-CoA synthetase; G3P, glycerol-3-phosphate; GPAT, G3P acyltransferase; LPA, lysophosphatidic acid; AGPAT, acylglycerol-3-phosphate acyltransferase; PhA, phosphatidic acid; PAP, phosphatidate phosphohydrolase; DAG, diacylglycerol; DGAT, diacylglycerol transferase; TAG, triacylglycerol; LD, lipid droplet; ER, endoplasmic reticulum.

Furthermore, exogenously supplied saturated and unsaturated FAs have differential effects on cells. Excess levels of palmitic acid (PA), a saturated FA, induces inflammation, ER stress, and ultimately cell death (*12–14*). Conversely, excess oleic acid (OA), an unsaturated FA, while inducing steatosis, does not cause the same toxic effects and even suppresses PA-induced apoptosis in cells (*13*, *14*). These effects are also evidenced in the resulting LD morphology. While both FAs cause an increase in LD size in comparison to control conditions, LDs resulting from OA feeding are often bigger than LDs in PA-fed cells. Meanwhile, PA-feeding causes a larger increase in the number of LDs per cell than OA-feeding (*14*, *15*). This suggests that PA and OA trigger a spatial regulation of lipid metabolism involving LD morphology. While it is known that various FAs conversely contribute to cell fates and liver disease, missing is a mechanistic understanding of how such disruptors affect localized metabolism at the sub-cellular level. Several theories have emerged. One theory is that PA's toxicity is due to its lower incorporation into LDs, changing the ratio of esterified to toxic unesterified FAs (*13*, *16*). Others attribute PA's toxicity to downregulation of TAG synthesis enzymes contributing to metabolic dysfunction (*17*). Thus, investigating PA localization and metabolism at a subcellular level is essential for understanding its role in disease.

Here, we leverage the sub-micron resolution of optical photothermal infrared (OPTIR) imaging to track PA metabolism in live hepatocytes (**Fig. 2A**). We have previously used OPTIR to track DNL and to monitor the effect of OA on DNL (*11*, *18*). In this work, we feed deuterated palmitic acid (PA-d_{31}, ^{2}H PA) to the hepatocyte-derived cell line Huh-7 and use C-D stretches and ester carbonyl shifts to monitor FA uptake, metabolism, and incorporation into LDs. Our results support both the theory that PA alters storage of FAs in LDs and downregulates TAG synthesis. Compared to OA, we observe slowed PA metabolism in the ER near LDs with abnormal morphology. We find that the two effects are coupled to phase changes in the ER that induce ER stress. Using the C-D stretches of ^{2}H PA we demonstrate that upon PA feeding, TAG precursors in the G3P pathway enter a rigid gel phase by tightly packing their acyl chains. Using the C=O stretch of ^{2}H PA we assign the TAG precursor to DAG. We conclude that acyl chain packing slows metabolism, leading to the buildup of DAGs in the ER, which in turn inhibits the ability of LDs to properly emerge from the ER, giving them an abnormal morphology. Azido PA, which packs less tightly than PA due to the azide, did not exhibit any of these effects. Similarly, unsaturated FAs like OA that have lower melting temperatures have been found to rescue cells from PA-induced apoptosis. Overall, this work sheds light on the toxic origins of PA and other saturated fatty acids, as well as establishes tools for understanding PA chemistry in the ER and the function of LDs in lipotoxicity.

Results

Palmitic acid feeding reveals an unanticipated spectral feature at 1734 cm^{-1}

To observe how PA is taken up and stored by the cell, we fed cells 60 μM ^{2}H PA conjugated to BSA at a 2:1 ratio, in line with physiological free fatty acid concentrations that fluctuate from submillimolar to millimolar (*19*, *20*). Cells were fed ^{2}H PA once at time 0 and were not refed throughout the duration of the experiments. Deuteration of the C-H bonds in PA shifts the frequency of the asymmetric and symmetric C-H_2 stretching modes from 2916 cm^{-1} and 2850 cm^{-1} to 2198 cm^{-1} and 2098 cm^{-1}, respectively (**Fig. S1**). These C-D_2 stretches lie in the "cell silent region", enabling detection of exogenously obtained PA without interfering signals from endogenously synthesized PA or other cellular molecules. Importantly, the ^{2}H does not alter the structure of PA and, therefore, it accurately mimics

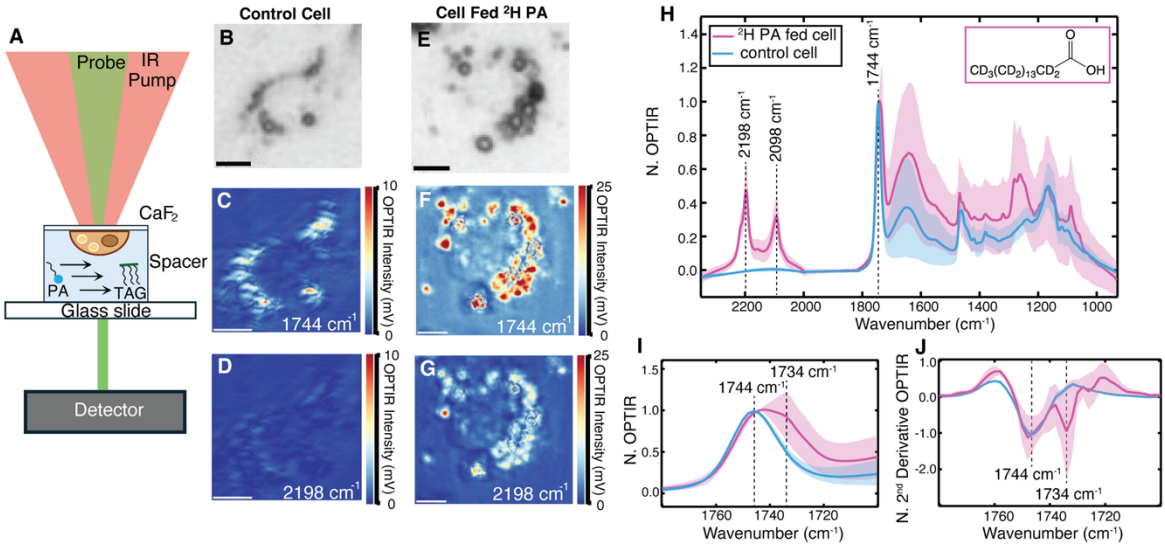

Fig. 2. Huh-7 cells fed ^{2}H PA exhibit an unanticipated shoulder off the C=O ester carbonyl stretch of TAGs/CEs. (**A**) Schematic of live cell imaging using OPTIR. (**B**) Brightfield of a live control Huh-7 cell. (**C**) Single wavenumber image of the control cell collected at the C=O lipid carbonyl band (1744 cm^{-1}). (**D**) Single wavenumber image of the control cell collected at the ν_{as} C-D$_2$ stretching mode (2198 cm^{-1}). (**E**) Brightfield of a live Huh-7 cell 24 hours after feeding 60 µM of ^{2}H PA conjugated to BSA at a 2:1 ratio. (**F**) Single wavenumber image of the ^{2}H PA fed cell collected at the C=O lipid carbonyl band (1744 cm^{-1}). (**G**) Single wavenumber image of the ^{2}H PA fed cell collected at the ν_{as} C-D$_2$ stretching mode (2198 cm^{-1}). (**H**) Average of 20 normalized OPTIR spectra collected across 20 LDs of 4 control Huh-7 cells (blue) and average of 20 normalized OPTIR spectra collected across 20 LDs of 4 ^{2}H PA-fed Huh-7 cells (pink). PA-fed cells were imaged 24 hours after feeding 60 µM of ^{2}H PA conjugated to BSA at a 2:1 ratio. Shading is one standard deviation of the average normalized spectrum. The dominant C=O peak at 1744 cm^{-1}, attributed to the ester carbonyl of TAGs/CEs, confirms that both cells are imaged on LDs. Only the cell fed ^{2}H PA exhibits C-D$_2$ asymmetric and symmetric stretches at 2198 cm^{-1} and 2098 cm^{-1}, respectively. (**I**) A closeup of the C=O spectral region from 1700 to 1780 cm^{-1}. An unanticipated shoulder at 1734 cm^{-1} is observed only in ^{2}H PA fed cells. (**J**) A second derivative of the C=O region further resolves the shoulder at 1734 cm^{-1}.

PA. Nor does the deuteration of PA affect cell viability at physiological free fatty acid concentrations (**Fig. S2A-C**). Further, the carbon chains are preserved as PA is metabolized, primarily through esterification and storage in LDs, allowing assignment of any species with these peaks as a derivative of ^{2}H PA. Free PA is generally not observable outside of LDs due to the detection limit of the instrument (**Fig. S3A-F**), in line with reported detection limits of similar instruments (*11*, *21*).

As most FAs end up esterified in LDs, initial spectra were collected on LDs of live Huh-7 cells 24 hours after feeding. Single wavenumber images were collected at frequencies attributed to ^{2}H lipids to confirm the uptake of ^{2}H PA. Control cells only fed BSA (vehicle control, **Fig. 2B**) only show signal in IR images collected at 1744 cm^{-1}, originating from the ester carbonyl stretch of TAGs and cholesteryl esters (CEs) in the LDs (*22*) (**Fig. 2C**). No signal is seen in IR images collected at 2198 cm^{-1}, the asymmetric C-D$_2$ stretch that would indicate a ^{2}H lipid (**Fig. 2D**). Cells fed ^{2}H PA (**Fig. 2E**) show signal in IR images collected at both 1744 cm^{-1} and 2198 cm^{-1} that overlap well with each other as well as the LDs in the brightfield, indicating that the ^{2}H PA has been taken up by the cell, esterified, and stored in

LDs (**Fig. 2F-G**). This is also confirmed by the strong C-D stretches in single spectra collected on LDs of ^{2}H PA-fed cells (**Fig. 2H**). Intriguingly, a 1734 cm^{-1} shoulder off this ester carbonyl peak (**Fig. 2I**) was observed in numerous PA-fed spectra. A second derivative further resolves this peak from the nearby 1744 cm^{-1} band (**Fig. 2J**). This spectral feature is only found in lipid-rich regions of cells fed ^{2}H PA and is always associated with C-D stretches, suggesting that it is a derivative of PA and therefore a lipid. To confirm that the shoulder is not an optical artifact derived from the deuterium labels on the PA, unlabeled PA was fed to cells at the same concentration and the same shoulder was observed (**Fig. S4A&B**).

Timelapse of the 1734 cm-1 peak suggests a metabolic intermediate

We hypothesize that the 1734 cm^{-1} shoulder arises from a metabolic intermediate of PA in the G3P pathway that generates TAGs. If true, there would be a temporal component to the C=O stretch as the ^{2}H PA is processed and not refed. To test this hypothesis, Huh-7 cells were incubated with ^{2}H PA and monitored by OPTIR approximately every three hours for 70 hours. An average of 77 spectra per timepoint were collected in LDs from approximately six cells per time point (total n=133) and each cell's corresponding spectra averaged. Spectra were collected by linescans with a spacing of approximately 300-500 nm or individual points on multiple LDs. This revealed a temporal trend to the 1734 cm^{-1} shoulder.

Throughout 72 hours, the LDs of cells grew with increasing time (**Fig. 3A-F**). For the first 12 hours, the 1744 cm^{-1} ester carbonyl peak of TAGs/CEs dominates the lipid region in the spectra. The peak at 1734 cm^{-1} first emerges as a small shoulder off the 1744 cm^{-1} peak around 12 hours after initial feeding (**Fig. 3G**). There was cell to cell heterogeneity in the exact time post-feeding that the shoulder presented, consistent with our past work that lipid metabolism is highly heterogeneous between cells (*11*, *18*). Over the next few hours, the intensity of the 1734 cm^{-1} band slowly increased until it was the dominating species in the ester carbonyl region. Between 27 and 54 hours the 1734 cm^{-1} peak was visible in almost all investigated cells. After which, it slowly merges back into the 1744 cm^{-1} peak between 52 and 70 hours after feeding. By 69 hours after feeding, the 1734 cm^{-1} peak is undetectable **Fig. 3G**). Averaged spectra from all cells in each timepoint in this experiment show the same trend **(Fig. S5A)**. Taking the second derivative of the averaged spectra confirms this trend (**Fig. 3H**), with the 1734 cm^{-1} peak appearing around 12 hours post-feeding, growing and predominating over the 1744 cm^{-1} stretch, and shrinking until it is indistinguishable from the 1744 cm^{-1} triacylglycerol peak by 69 hours post-feeding. This is also confirmed by taking the second derivative of the averaged spectra of all cells in each timepoint of this experiment (**Fig. S5B)**. Additionally, the distribution of 1734 cm^{-1} intensity of all spectra in each timepoint shows the spread of increasing and decreasing 1734 cm^{-1} intensity throughout time. (**Fig. S5C)**.

This data is consistent with our hypothesis, that the unknown lipid peak is a metabolic intermediate that is built up to a concentration detectable via OPTIR over the first 27 hours, and then processed to a concentration undetectable via OPTIR over the following 42 hours. Further, from 12 to 27 hours, the second derivative reveals additional peaks at 1726 and 1738 cm $^{-1}$ that indicate low populations of other metabolic intermediates (**Fig. 3H**).

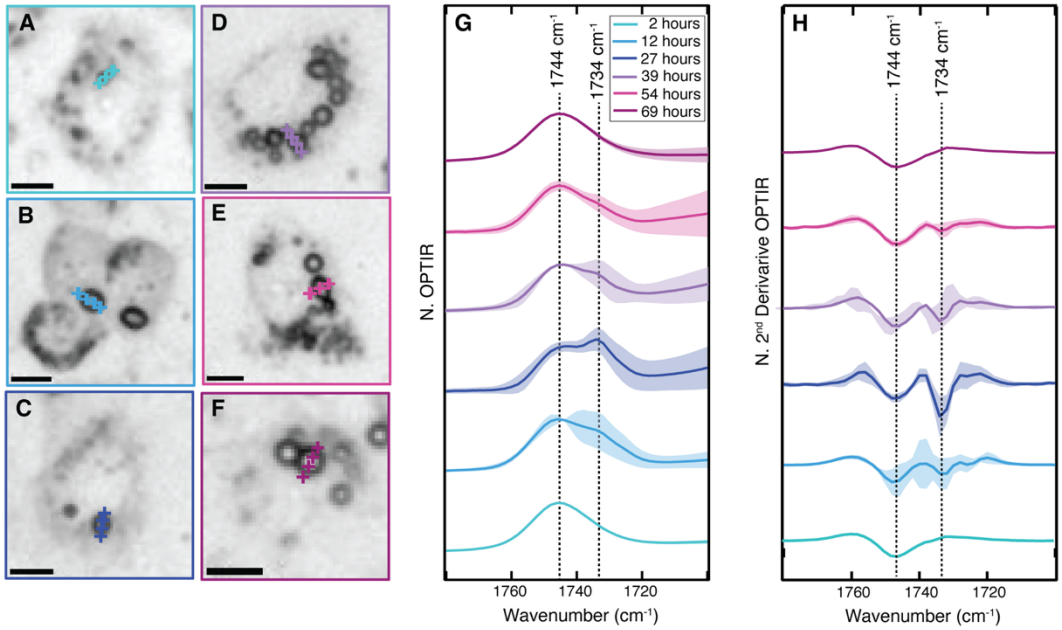

Fig. 3. Timelapse of the ester carbonyl stretch region from 2 to 70 hours post feeding 60 µM ^{2}H PA conjugated to BSA at a 2:1 ratio illustrated by spectra from cells representing the average data with 1734 cm^{-1} shoulder. (**A-F**) Brightfield images of representative Huh-7 cells fed at 2, 12, 27, 39, 54, and 69 hours, respectively. Colored crosses indicate linescans where corresponding spectra were collected and is plotted in (G). Scale bars are 10 µm. (**G**) Average normalized IR spectra with standard deviation of Huh-7 cells fed ^{2}H PA at 2, 12, 27, 39, 54, and 69 hours. Each time point represents the average spectra from the points labeled in (A-F). Shading is one standard deviation of the average normalized spectrum. (**H**) Second derivative of the average spectra in (G) with corresponding standard deviations.

Intermediate buildup occurs in the ER

Brightfield images reveal changes in the morphology of ^{2}H PA-fed cells. LDs in cells fed ^{2}H PA increased in both size and number compared to control cells (**Fig. 4A**). This observation agrees with other studies that report PA induces an increase in LD size and number (*14*, *23*). In addition to this, LD morphology is altered; many LDs in PA fed cells are oblong shape (**Fig. S6A-B**). LD morphology was quantified in 50 LDs from control or PA-fed cells; consistent with our qualitative observations the ellipticity of PA-fed cells is 0.8 ± 0.1 and control cells is 0.94 ± 0.06 (**Table S1**). These oblong LDs tend to have strong 1734 cm^{-1} signal and are only observed when feeding PA, not in control conditions nor when feeding unsaturated FAs such as OA (**Fig. S6C-F)**. Abnormal LD morphology in combination with the hypothesis that the 1734 cm^{-1} intermediate species is from TAG synthesis suggests that the buildup of these intermediates affects how LDs bud from the ER.

LDs have many contact points with other organelle, including the ER, mitochondria, and peroxisomes (*4*, *24*). These contact points form metabolic hubs imperative to FA homeostasis and facilitate FA trafficking, contributing to LD growth and degradation (*4*, *24*). We focus on the ER because TAG synthesis and LD nucleation occur in the ER. ER-LD contact sites are typically 10-80 nm, which are below the sub-500 nm spatial resolution of the OPTIR (*25*). Nevertheless, OPTIR can test our hypothesis that intermediate buildup in the ER affects how LDs bud from the ER; OPTIR can resolve whether the intermediate occurs in LDs colocalized with the ER, whether it is isolated to the ER or LD, and whether the LD has abnormal morphology. As we believe the 1734 cm^{-1} peak is a ^{2}H PA metabolite,

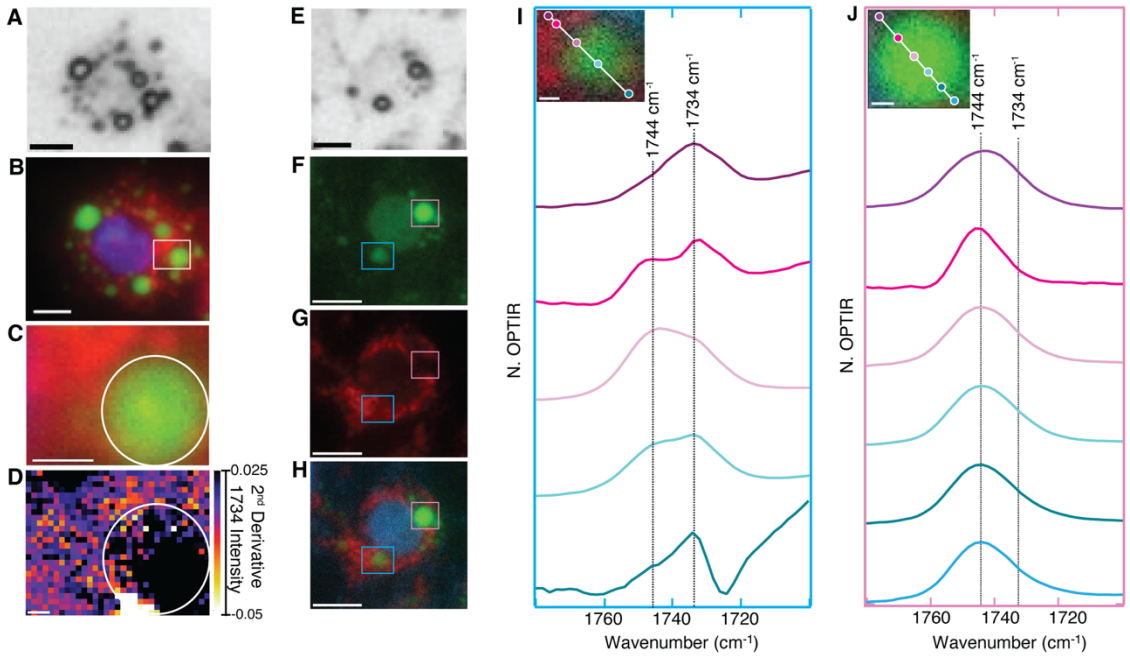

Fig. 4. PA intermediates build up in the ER. (**A**) Brightfield image of a cell 24 hours after feeding with 120 µM of ^{2}H PA conjugated to BSA at a 2:1 ratio. Scale bar is 10 µm. (**B**) Fluorescence image of the cell in (A) stained for the ER (red), nucleus (blue), and LD (green). A white box indicates where a hyperspectral image was collected. Scale bar is 10 µm. (**C**) Fluorescence signal in the region where the hyperspectral image was collected. The LD is outlined in white. Scale bar is 1 µm. (**D**) Single wavenumber image of the second derivative of the 1734 cm^{-1} band in the hyperspectral image with the LD outlined in white. **(E)** Brightfield image of a cell 24 hours after feeding with 120 µM of ^{2}H PA conjugated to BSA at a 2:1 ratio. (**F**) The green fluorescence channel of the cell in (E) stained for LD. Pink and blue boxes indicate the LDs that were studied. Scale bar is 10 µm. (**G**) The red fluorescence channel of the cell in (E) stained for ER. Pink and blue boxes indicate the LDs that were studied. Scale bar is 10 µm. **(H)** The cell in (E) stained for the ER (red), LD (green), and nucleus (blue). Pink and blue boxes indicate the LDs that were studied. Scale bar is 10 µm. **(I)** Spectra corresponding to the points where a linescan was collected across the LD in the blue box (inset). Lipid bands at 1744 cm^{-1} and 1734 cm^{-1} are marked. Scale bar is 1 µm. (**J**) Spectra corresponding to the points where a linescan was collected across the LD in the pink box (inset). Lipid bands at 1744 cm^{-1} and 1734 cm^{-1} are marked. Scale bar is 1 µm. All images collected on the OPTIR.

it should increase in intensity when the concentration of ^{2}H PA fed to cells is increased. Thus, to better resolve the shoulder, Huh-7 cells were incubated with ^{2}H PA at a slightly higher physiological concentration of 120 µM conjugated to BSA at a 2:1 ratio. After 24 hours, cells were fluorescently stained for the nucleus, ER, and LD with Hoechst nuclear stain (blue), ER-Red (red), and LipiSpot (green), respectively. Cells were then imaged live on the OPTIR. Cells with multiple, large LDs were chosen for analysis (**Fig. 4A**).

To determine if the 1734 cm^{-1} peak is associated with the ER and/or spatially confined to the LDs, hyperspectral images were collected across LDs in regions with high ER fluorescence (**Fig. 4B-D**). Hyperspectral maps are three-dimensional images comprised of OPTIR spectra from 1600 to 2348 cm^{-1} collected at every pixel within the area of interest. From a hyperspectral map, a single wavenumber image of the second derivative of the 1734

272 cm^{-1} peak reveals the spatial distribution of the metabolic intermediate relative to
273 TAGs/CEs. Higher 1734 cm^{-1}/1744 cm^{-1} ratios are found both at the edge of LDs bordering
274 the ER and in the ER itself (**Fig. 4D**). This indicates that the metabolic intermediate is
275 concentrated in the ER and likely near LD-ER contact sites. Still, to rule out that the 1734
276 cm^{-1} peak originates from the ER itself rather than a metabolic intermediate, a control cell
277 was stained for the ER, nucleus, and LD and imaged live on the OPTIR (**Fig. S7A-B**). 1744
278 cm^{-1} is only detected at the center and edge of the LD, and only amide I and water signal
279 are present in the ER (**Fig. S7C**).
280
281 To further confirm that the intermediate is arising from chemistry in the ER, a cell with both
282 a LD in an ER rich region and a LD in an ER free region was investigated (**Fig. 4E**). This
283 was confirmed by separating the red, green, and blue fluorescence channels to identify LDs
284 with high overlap with the ER (**Fig. 4F-H)**. Linescans were collected over LDs with high
285 or low ER overlap. (**Fig. 4I-J**). Like the droplet in **Fig. 4A**, the LD with potential to make
286 ER contacts had regions of increased 1734 cm^{-1} intensity at the LD edge bordering the ER.
287 At the edges of the LD the 1734 cm^{-1} band dominates, while the 1744 cm^{-1} band dominates
288 in the center of the LD (**Fig. 4I**, full spectra in **Fig. S8A**). The 1734 cm^{-1} peak persisting
289 throughout the center of the LD likely originates from DAGs in the ER surrounding the LD,
290 as there is high red fluorescence overlap with this LD. In contrast, the LD in an area without
291 potential to make ER contacts (**Fig. 4H**) did not have any regions with strong 1734 cm^{-1}
292 signal (**Fig. 4J**, full spectra in **Fig. S8B**), indicating that there are no metabolic intermediates
293 building up in or around that LD. This LD also did not have high fluorescence overlap,
294 indicating it is further from the ER where DAGs buildup. This further highlights the
295 heterogeneity of the LDs within cells, as some exhibit this 1734 cm^{-1} lipid species and some
296 do not. This trend was confirmed through complementary fluorescence and infrared analysis
297 of a total of 8 LDs; only LDs in ER rich regions have the 1734 cm^{-1} signal, and thus
298 metabolic intermediate buildup (**Fig. S9A-P**). As TAG synthesis occurs in the ER and LDs
299 are known to have multiple contacts with the ER even after budding, we hypothesize that
300 the 1734 cm^{-1} lipid species is a precursor of TAG synthesis arising from PA feeding.
301
302 **DAGs accumulate in Huh-7 cells upon PA feeding**
303 Previous work has shown that lipid metabolism is affected by PA feeding (*17*, *26*, *27*). Cells
304 fed PA tend to have large increases of glycerolipids in comparison to control conditions.
305 Specifically, lipodomics find that large amounts of disaturated DAGs accumulate (*26*, *27*).
306 We hypothesize that the 1734 cm^{-1} lipid species is a disaturated DAG building up to a
307 concentration that is observable by OPTIR.
308

309 TAG synthesis by the G3P pathway includes five primary lipid species: a free fatty acid,
310 LPA, PhA, DAG and TAG (**Fig. 5A**). To assign the 1734 cm^{-1} peak, we compare it to the
311 OPTIR spectra of these five lipid species. As we established the unassigned dominant
312 intermediate arises from PA feeding, the acyl chains of all TAG precursors analyzed were
313 solely comprised of PA. IR spectra for palmitic acid, palmitoyl lysophosphatidic acid, 1,2-
314 dipalmitoyl-sn-glycero-3-phosphate, 1,2- dipalmitoyl-sn-glycerol, and tripalmitin were
315 collected on the OPTIR. However, the vibrational frequency of a bond, especially carbonyls,
316 is dependent on the local electric field as well as nearby hydrogen bonds (*28*). Thus, the
317 spectrum of each lipid species may differ slightly depending on the solvent. Previous work
318 has shown that the ER has a polarity between chloroform and dichloromethane (DCM) (*29*).
319 Therefore, to replicate the polarity of the ER, all five precursors were dissolved in

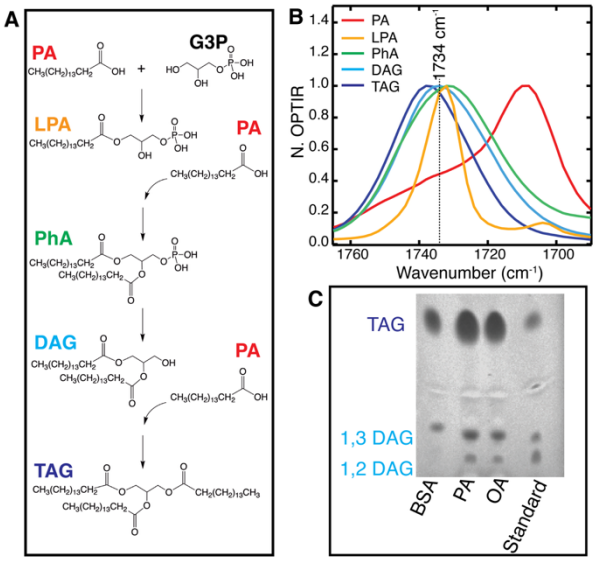

Fig. 5. Assignment of 1734 cm^{-1} to DAGs. (**A**) TAG synthesis via the G3P pathway with PA as the FA chains. (**B**) OPTIR spectra of TAG intermediates dissolved in chloroform at 25 mM. (**C**) TLC plate of lipids isolated from PA-fed, OA-fed, and control cells. Cells were fed 60 µM of BSA-conjugated PA or OA or BSA alone (control) and incubated for 24 hours. Tripalmitin (TAG), 1,3 dipalmitin (1,3 DAG), and 1,2 dipalmitin (1,2 DAG) were used as standards.

chloroform at a concentration of 25 mM (**Fig. 5B**). The solubility of PhA and LPA in DCM was below the detection limit of the OPTIR, therefore, only PA, DAG, and TAG were compared in DCM (**Fig. S10**). Comparing the OPTIR spectra in chloroform, the carboxylic acid carbonyl of PA is at 1709 cm^{-1}, while the rest of the precursors have ester carbonyls with peaks that are in the range of 1730-1740 cm^{-1}. As anticipated, the bandwidth and peak position of the ester carbonyl of DAGs in chloroform best matches the *in cellulo* peak at 1734 cm^{-1}. In DCM, DAG appears at 1736 cm^{-1}, also closely matching the 1734 cm^{-1} peak. Thus, we assign the 1734 cm^{-1} peak to DAGs.

To further confirm the DAG assignment the cell's lipid profile was assessed using thin layer chromatography (TLC). Cells were incubated with 60 µM of BSA-conjugated PA or OA or BSA alone (vehicle control) for 24 hours. Lipids were then isolated from the cell using the Bligh and Dyer lipid extraction technique and spotted onto TLC plates (**Fig. 5C**). In comparison to control cells fed BSA, PA- and OA-fed cells both produced large amounts of TAGs and 1,2 DAGs. This partially agrees with a previous study that used TLC to separate lipid extracts from cardiomyoblasts, however, in cardiomyoblasts PA led to the formation of significantly more DAGs than OA (*30*). The TLC plate was quantified and PA-fed cells had 4.4% of the 1,2-DAGs in the total lipid profile, while OA-fed cells had 3.1% of 1,2-DAGs in the lipid profile, resulting in 1.4 more 1,2-DAGs in the PA-fed cells than in OA-fed cells. In hepatocytes, the increase in DAGs upon PA- and OA-feeding is not as drastic (**Fig. 5C**). This is interesting as DAGs are only easily detected using OPTIR on PA-fed hepatocyte cells, suggesting that they are more evenly distributed across the ER (below the detection limit) of OA-fed hepatocyte cells. We previously used the same OPTIR approach to monitor ^{2}H OA feeding in hepatocytes and adipocytes, and no such TAG precursor peak had been observed (*11*). To further investigate, Huh-7 cells were fed 60 µM of ^{2}H OA conjugated to BSA at a 2:1 ratio to match the PA time-dependent study. Cells fed ^{2}H OA were then studied using OPTIR throughout 24-48 hours. Linescans were collected through

large LDs. Surprisingly, a few LDs exhibited a shoulder at 1738 cm^{-1} off the 1744 cm^{-1} carbonyl stretch (**Fig. S11A**). Although this peak was found in OA-fed cells, it was far less common (**Fig. S11B**). Furthermore, no LDs with abnormal morphology were observed (**Fig. S11C-D**). This suggests that similar amounts of TAGs and DAGs are present in both PA- and OA-fed Huh-7 cells, but their spatial distributions and cell phenotypes differ. That DAGs are infrequently detected by OPTIR in OA-fed Huh-7 cells indicates that they are distributed across the cell such that the local concentration is below the detection limit of the OPTIR. Thus, another factor exists that is contributing to the large local buildup of DAGs in the ER of PA-fed Huh-7 cells.

ER rigidity is correlated with metabolic inhibition

A physical difference between OA and PA is their melting temperature. In general, saturated fats have higher melting temperatures than unsaturated fats because their straight acyl chains can be tightly packed. Indeed, the melting temperature of OA is ~13 ºC, while the melting temperature of PA is ~63 ºC (*31*). This trend is maintained through the five primary lipid species in TAG synthesis; the melting temperature of triolein is ~5 ºC while the melting temperature of tripalmitin ~45-66 ºC (*31*, *32*). Thus, at physiological temperatures OA and its TAG intermediates are a liquid whereas PA and its TAG intermediates are a solid. Mixtures of FAs have lower melting temperatures than pure FA (*33*), however, FA feeding artificially inflates the cellular distribution of the fed FA. We therefore hypothesize that PA and its TAG intermediates solidify in the ER, leading to ER stress and DAG accumulation.

To test this hypothesis, we investigate the C-D stretches of the acyl chains. As described above, differences in solvent polarity were considered in the assignment of the shifted lipid carbonyl peak. However, other physical properties of lipids can alter vibrational spectra, most notably the conformation and structure of the lipid (*34–36*). Lipids are polymorphic and under physiological conditions can undergo a lamellar gel to lamellar liquid-crystalline phase transition. The lamellar gel state is characterized by fully extended and rigid acyl chains in an all-*trans* conformation, resulting in ordered and tightly packed lipids (*34*). In contrast, the lamellar liquid-crystalline state is a disordered environment, with more hydrocarbon chains in the *gauche* conformation, allowing for increased dynamics of lipid molecules (*34*). Previous studies have demonstrated that the C-H vibrational modes can distinguish between these two states (*37*, *38*). The liquid crystalline phase is characterized by higher frequencies and broadening of the CH_2 bands due to the increase in dynamics between acyl chains.

The C-D vibrational modes of Huh-7 cells were imaged by OPTIR 24 hours after ^2H PA feeding. There is a stark difference between the symmetric and asymmetric CD_2 stretches in spectra with and without the 1734 cm^{-1} lipid carbonyl peak. In an OPTIR spectrum taken on a LD far from the ER, the 1744 cm^{-1} lipid carbonyl dominates. Consistent with a liquid-crystalline phase, the corresponding symmetric and asymmetric CD_2 stretches are located at 2098 cm^{-1} and 2200 cm^{-1}, respectively (**Fig. 6A, bottom**). These are TAGs made with ^2H PA acyl chains esterified and stored in LDs. When focused on the edge of a LD near the ER, the 1734 cm^{-1} peak dominates the lipid carbonyl region and the symmetric and asymmetric CD_2 stretches redshift to 2090 cm^{-1} and 2194 cm^{-1}, respectively (**Fig. 6A, top**). This is consistent with ^2H PA acyl chains in a lamellar gel phase. Further, a small peak appears at 2158 cm^{-1}, which can be assigned as Fermi resonance between the symmetric CD_2 mode and the first overtone of the CD_2 bending mode (**Fig. 6B**) (*37*, *39*, *40*). Fermi resonant interactions are sensitive to conformational changes of a molecule and have been used to monitor intermolecular interactions (*41–43*). This particular Fermi resonance has

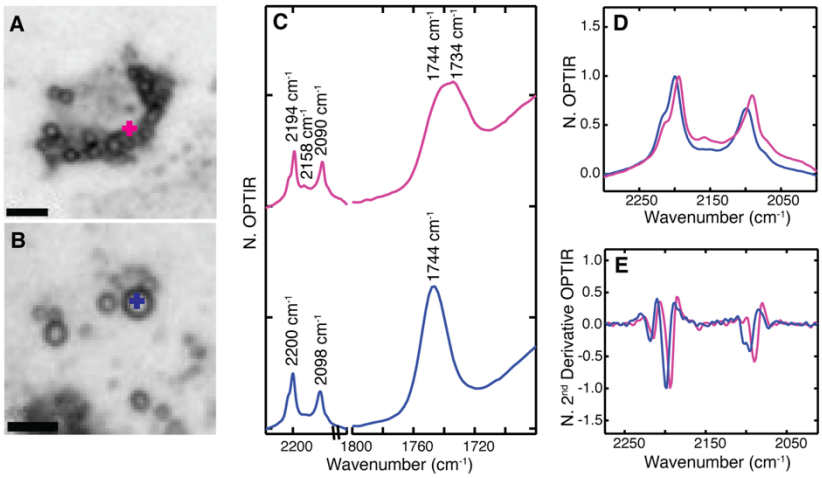

Fig. 6. 1734 cm^{-1} signal appears in an ordered lamellar gel environment. (**A**) Brightfield image of a Huh-7 cell fed 60 µM of ^{2}H PA conjugated to BSA at a 2:1 ratio. The spectrum was collected as a single spectrum on the edge of a LD near the ER 24 hours after being fed ^{2}H PA (indicated by the pink crosshairs). **(B)** Brightfield image of a Huh-7 cell fed 60 µM of ^{2}H PA conjugated to BSA at a 2:1 ratio. The spectrum was collected as a single spectrum on the center of a LD of a cell 69 hours after being fed ^{2}H PA (blue crosshairs). (**C**) A redshift of the asymmetric and symmetric CD_2 stretches and the appearance of a Fermi resonance at 2158 cm^{-1} is correlated with the appearance of a 1734 cm^{-1} shoulder off the lipid carbonyl. Enlarged view of the C-D region and its corresponding second derivative spectra is shown in (**D**) and (**E**), respectively. Measurement of multiple cells and samples produced the same results. Spectra were normalized by prominent peak heights in the C-D region.

been reported to disappear during the lipid transition from the ordered lamellar gel phase to the liquid crystalline phase (*37*, *44*). Second derivative spectra confirm the appearance of the Fermi resonance as well as the shifting of the CD_2 peaks (**Fig. 6C**). These results are reproducible across multiple spectra with and without the 1734 cm^{-1} peak. In most cases, the dominance of the 1734 cm^{-1} peak in the lipid carbonyl region is associated with a CD_2 redshift and the appearance of the Fermi resonance. As previously established, these spectral features are most common at the edges of a LD colocalized with the ER. Thus, as hypothesized, we conclude that it is lipids in the ER that are forming a lamellar gel state due to the incubation of PA which creates tighter packing of the acyl chains of TAG precursors in the ER. Most biomembranes, including the ER membrane, exist in the liquid crystalline state to allow for diffusion of biomolecules (*45*). We further speculate that enzymatic reactions necessary for TAG synthesis are diffusion limited in the lamellar gel state, slowing PA metabolism. To investigate this, FRAP was performed on control cells and cells fed 120 µM of ^{2}H PA using an ER-mEGFP plasmid that localizes to the ER. The fluorescence recovery of control and PA-fed cells was similar. We determined diffusion times from the resulting FRAP curves and identified a diffusion time of 3 ± 1 seconds for control cells and diffusion time of 8 ± 1 seconds for ^{2}H PA-fed cells (**Fig. S12)**. This further confirms that metabolites building up in the ER promote ER rigidity and affects enzyme mobility.

In addition to C-D stretches, azides are particularly sensitive to local environmental changes (*46*, *47*). To gain further insight into the environmental changes that occur in the ER upon PA build up, cells were fed 120 µM of azido PA. The azide peak appears at 2196 cm^{-1} in the cell silent region and is expected to redshift upon exposure to a nonpolar environment. However, no 1734 cm^{-1} lipid peak was found in any cells fed azido PA and the azide signal

434 was only observed in LDs (**Fig. S13**). This suggests that azido PA TAG precursors do not
435 build up and form a lamellar gel state in the ER like ^{2}H PA and unlabeled PA. Unlike
436 deuteration, which preserves the PA structure, incorporation of an azide slightly modifies
437 the PA structure. Azido PA has a bulky azide group on the end of the hydrocarbon tail,
438 which increases the area per molecule, reducing lipid thickness and restricting how closely
439 molecules can pack together. Thus, our measurements suggest that azido PA has a melting
440 point below PA and below physiological, 37 ºC. Azide FAs have widely been used in
441 vibrational studies, yet, to our knowledge, the 1734 cm^{-1} shoulder has never been reported
442 (*48*, *49*). This presents a pitfall in the use of azido FAs as the azide modification affects FA
443 metabolism. In addition, this observation confirms the correlation between the lamellar gel
444 state and DAG accumulation.
445
446 To further investigate the extent of this effect, 120 µM of a 1:10 mixture of azido PA to
447 unlabeled PA was fed to cells and imaged 24 hours after feeding. Similarly, no 1734 cm^{-1}
448 lipid peak was found in any cells. This suggests that even low concentrations of azido PA
449 disrupt lamellar gel state formation. It is well established that OA prevents PA-induced
450 apoptosis. Ratios of OA to PA ratios as low as 1:25 have been recorded to have a protective
451 effect against PA-induced apoptosis (*13*, *16*, *50*). Unsaturated long chain FA have lower
452 melting temperatures and exist as liquids at room temperature. We hypothesize that the
453 double bond of OA, similarly to the relatively bulky azide group of azido PA, disrupts
454 formation of the lamellar gel state in the ER resulting in unrestricted movement in the ER,
455 maintaining metabolic flux, and sequestering FAs into LDs to prevent apoptosis.
456
457 As reported above, a few Huh-7 cells fed ^{2}H OA exhibited shifts in their ester carbonyl
458 consistent with buildup of metabolic intermediates. To investigate whether this was
459 correlated with a change in the state of the ER, 60 µM ^{2}H OA was fed to Huh-7 cells that
460 were monitored by OPTIR approximately every three hours for 70 hours. As anticipated,
461 the majority of ^{2}H OA-fed cells do not exhibit any lipid carbonyl shoulders or shifts.
462 However, as previously observed, a few cells do exhibit broadening and shifts of lipid
463 carbonyl peaks and corresponding CD_2 shifts, indicating that there is a buildup of
464 metabolites and a phase change near LD embedded in the ER (**Fig. S14A-C**). Still, this shift
465 was found less frequently in OA-fed cells compared to PA-fed cells. When considering
466 averaged spectra of all cells in each timepoint, there is no trend of 1734 cm^{-1} buildup (**Fig.
467 S15A**). Nor is there a consistent trend in the averaged second derivative spectra (**Fig. S15B**).
468 The spread of 1734 cm^{-1} intensity of all spectra per timepoint also does not have an obvious
469 increasing and decreasing trend that is seen in ^{2}H PA fed cells (**Fig. S15C**).
470
471 To quantify this, all spectra in the OA- and PA-fed timelapse experiment where cells were
472 fed 60 µM PA or OA conjugated to BSA at a 2:1 ratio and imaged every three hours were
473 analyzed. In total each timelapse experiment included over 100 cells, 400 lipid droplets, and
474 1500 spectra (**Table S2&S3**). A spectrum was considered to have a lipid carbonyl shift if
475 there was a shoulder at 1738 cm^{-1} or below, after a background subtraction by shifting the
476 baseline toward zero by subtracting a constant value of the intensity at 1816 cm^{-1} and
477 normalizing the spectrum to 1744 cm^{-1}. Between the timepoints of 1-70 hours, 40% of PA-
478 fed cells and 23% of PA-fed LDs exhibited a lipid carbonyl shift in at least one spectrum,
479 compared to 14% of OA-fed cells and 5% of OA-fed LDs (**Table S2&S3**). Of the cells that
480 exhibited the lipid carbonyl shift, 50% of PA-fed cell spectra had shifts, compared to 24%
481 of OA-fed cell spectra. Generally, hepatic LDs contain more TAGs than CEs (*51*, *52*). One
482 possibility is that CEs can also undergo a phase transition, cholesteryl oleate and cholesteryl
483 palmitate have melting temperatures above physiological, ~44 ºC and ~76 ºC, respectively

484 (*53*, *54*). Thus, it stands that C-D shifts and DAG lipid carbonyl peaks are more common in
485 PA-fed cells, as both palmitate TAG precursors and cholesteryl palmitate have higher than
486 physiological melting temperatures. Only cholesteryl oleate has a higher than physiological
487 melting temperature in OA-fed cells, resulting in less common C-D shifts. This suggests
488 that not only are TAG precursors accumulating and forming a lamellar gel phase, but
489 cholesteryl esters contribute to this as well.
490
491 **Discussion**
492 Despite incredible advancements in understanding the roles LDs and PA play in metabolic
493 disorders, many techniques cannot sufficiently answer the outstanding questions in the field.
494 Lipidomics and biochemical assays have provided insight to how PA changes the FA profile
495 but are lacking in spatial information essential to connect these effects to the cell at a sub-
496 cellular level (*13*, *26*). Enzyme inhibition studies have spurred hypotheses on how PA
497 disrupts metabolism, but look only at a particular metabolic step rather than the entire
498 cellular system or trigger off-pathway compensations (*17*). Optical imaging is a promising
499 approach to spatially resolve cellular metabolism. Techniques including magnetic
500 resonance imaging and fluorescence imaging have made great progress in visualizing
501 cellular metabolism and have contributed to the development of drugs and disease prognosis
502 (*55*). However, these techniques have their own limitations, whether it be sensitivity,
503 suitability for dynamic imaging, or use of bulky and perturbative probes.
504
505 Vibrational microspectroscopy coupled with vibrational probes has the potential to be an
506 extremely powerful technique in the field of cell biology. Vibrational probes are small and
507 biorthogonal, allowing for their incorporation and detection amongst other exogenous
508 cellular molecules (*48*). Additionally, vibrational probes are environmentally sensitive
509 providing information on the physical properties of the cell, which are difficult to obtain
510 with conventional probes. As FAs are simple to label and easy for cells to uptake, many
511 vibrational studies have monitored FA metabolism. Raman microspectroscopy has analyzed
512 deuterated and alkyne-tagged PA's effect on cells and whole organisms (*36*, *56*). Shen *et al*.
513 used the Raman C-D vibrational mode along with fluorescent stains and HPLC-MS to
514 monitor the formation of solid-like domain separation in the ER induced by ^{2}H-PA feeding
515 in HeLa cells (*57*). However, like other Raman studies, they focus on the acyl chains, as C-
516 H bonds are particularly Raman active while carbonyl bonds are weak (*58*). This presents a
517 disadvantage of Raman imaging, as it is not possible to directly observe the chemistry that
518 occurs at the lipid headgroup during TAG synthesis.
519
520 IR is more sensitive to carbonyl bonds, and, with the recent development of sub-micron
521 OPTIR, IR imaging now provides sufficient resolution to probe carbonyl metabolism at the
522 sub-cellular level. Recent OPTIR studies used labeled PA but, like previous Raman studies,
523 focus on the C-H and C-D regions. Park *et al.* monitored neutral lipid synthesis in live cells
524 using ^{2}H PA, but did not report any spectral shifts in the ester carbonyl region of TAGs/CEs
525 (*21*). Shifts in the C-D region were attributed to heterogeneity of TAG acyl groups. While
526 this could partially contribute to the broadening and shifts that we observe, the fermi
527 resonance in our data is strong spectral evidence of a liquid crystalline to lamellar gel phase
528 change. Teng *et al*. report FA desaturation of ^{2}H PA through monitoring the vibration of the
529 unsaturated C-D bond (*59*). They do not report C-D shifts, and we do not observe an
530 unsaturated C-D bond vibration upon ^{2}H PA feeding, but this may be due to a difference in
531 cell lines. Bai *et al*. also monitored lipid synthesis over various model systems, but used
532 azido-PA, which we discover does affect FA metabolism by disrupting the formation of a
533 lamellar gel state (*49*). While these studies advanced the field, our work highlights the

importance of using probes that do not alter FA metabolism and that can directly monitor where the chemistry occurs, at the headgroup of the lipid.

DAGs are involved in many cellular functions, mostly as signaling molecules and precursors to glycerolipids (*60*). As a signaling molecule, it is thought that DAGs block insulin signaling, resulting in insulin resistance, a symptom of type 2 diabetes and hepatic steatosis, both of which are often simultaneously observed in patients (*61*, *62*). Thus, buildup of DAGs has been implicated in hepatic diseases, but the extent of its impact on PA lipotoxicity is still debated. Our evidence suggests that DAGs are a necessary component to PA lipotoxicity, as it is the longest lived lipid intermediate in the G3P pathway (**Fig. 3**). Previous work has implicated DGAT1, which converts DAGs to TAGs, as a reason for DAG buildup and inhibition of TAG synthesis (*17*, *27*). Unsaturated FAs are thought to be superior substrates for TAG synthesis, while saturated FAs and DAGs are thought to be poor substrates that impair cellular flux, leading to accumulation of saturated lipid species (*5*, *27*). This aligns well with other findings that have found PA is less likely to be esterified into LD compared to OA, most likely due to TAG inhibition from saturated substrates (*12*, *13*, *27*). While our measurements agree that there are spatial differences in the esterification of OA and PA into LDs, we find that they result in a comparative buildup of TAG intermediates (**Fig. 5C**). Further, we also see that OA and PA have similar effects to cell viability at 60 μM. It is not until later time points and higher concentrations that cell viability greatly differs, with PA causing more cell death than OA (**Fig. S16A-C**). This confirms that there may be similar effects occurring in the cell, but once the buildup of TAG intermediates becomes overloading, the differences between OA and PA become more drastic. We also find that both OA and PA have similar upstream effects on metabolic pathways. Consistent with our past OA studies, compared to control conditions, cells fed ^{13}C glucose and ^{2}H PA exhibit lower incorporation of ^{13}C in TAGs/CEs (**Fig. S17**) which we attribute to downregulation of DNL-associated enzymes (*11*). Rather than saturated substrates inhibiting TAG enzymes in the G3P pathway, our measurements point towards an alternate, physical mechanism as the origin of DAG buildup in the ER.

In the ER, the C-D stretches of PA derived intermediates were consistent with a lamellar gel state. As saturated lipids can pack tighter together than unsaturated lipids, increased membrane order induces ER stress (*26*, *63*). Many studies have linked PA to increased ER stress and in turn, poor cellular health (*17*, *26*, *64*). This is due to altered lipid composition of the ER, which disrupts homeostasis and ultimately activates stress responses (*63*, *65*). Normally, to combat this, TAG synthesis enzymes relocalize from the ER to the budded LD surface via membrane tethers (*66*). However, upon elevated DAG levels, LD remain embedded in the ER. The conical shape of DAGs have a negative intrinsic curvature, which disfavors budding and promotes an embedded state of LDs (*4*, *67*). Our findings support this model. DAGs were only seen at the edges of LDs co-localized with the ER, suggesting that these LDs were still embedded in the ER. Further, the oval shaped LDs that were observed imply that there are issues with proper budding. These were also the LDs that were more likely to accumulate DAGs. Furthermore, as azido PA cannot be packed as tightly as PA, it did not induce DAG accumulation. Similar effects are seen upon OA feeding. Numerous studies have reported that as little as 1:25 OA can reverse negative effects of PA (*13*, *14*, *50*). OA likely disrupts the packing of PA, thereby reducing ER stress due to its lower melting temperature and increased enzyme diffusion. Thus, it is a physical change rather than direct enzyme inhibition that gives rise to the altered PA metabolism. Although there are still many questions about LD growth and function, our findings contribute a

583 spatial understanding of the role PA chemistry and disaturated DAGs play in LD dynamics
584 and morphology.
585
586 Using OPTIR, we have visualized DAG accumulation upon PA feeding through the
587 emergence of a time-dependent ester carbonyl peak and monitored physical properties of
588 the ER through C-D stretches in the acyl chains. To our knowledge, this is the first time
589 TAG intermediates have been directly detected in live cells. Notably, this chemistry could
590 be tracked entirely label free. In addition, OPTIR allowed us to monitor lamellar gel and
591 liquid crystalline lipid states in the ER and LDs using shifts in the C-D region. Through
592 these observations, we have established a mechanism by which PA induces lipotoxicity in
593 the cell. As saturated PAs are imported to the ER for TAG synthesis, acyl chain packing of
594 PA and associated intermediates induces a phase change to an ordered lamellar gel state that
595 slows diffusion of enzymes necessary for TAG synthesis. ER stress occurs through the
596 accumulation of disaturated DAGs and other lipid intermediates as well as LDs embedding
597 in the ER. LD-organelle contact sites are disrupted as the LDs have not properly budded,
598 interfering with lipid metabolism. This provides insight to how PA induces lipotoxicity and
599 establishes OPTIR as a highly effective technique to monitor lipid metabolism.
600
601 **Materials and Methods**
602
603 **Materials**
604 Unless otherwise specified, all materials were sourced from Sigma-Aldrich.
605
606 **FA conjugation**
607 Fatty acid conjugation was performed as previously described using a protocol adapted by
608 Shi *et al* (*11*, *48*). Briefly, in a 2 mL clear glass container (VWR, Radnor, PA), ^{2}H palmitic
609 acid (palmitic acid-d_{31}, DLM 215, Cambridge Isotope Labs, Tewksbury, MA), or azido
610 palmitic acid (CCT 1346, Vector Laboratories, Newark, CT) was dissolved in 29 mM NaOH
611 and heated in a 70 ºC water bath until clear. The fatty acid solution was then diluted to a
612 total concentration of 3 mM with 150 mg/mL fatty-acid free BSA (MP Biomedicals, Santa
613 Ana, CA) dissolved in DPBS (Thermo-Fischer, Waltham, MA). The solution was heated
614 again at 37 ºC in a water bath until clear and filtered with a 0.2 um sterile filter. Final ratios
615 of palmitic acid to BSA were 2:1, in line with physiological ratios (*19*).
616
617 **Huh-7 cell culture**
618 Huh-7 cells (a gift from the Yale Liver Center) were cultured as previously described (*11*).
619 Briefly, cells were grown to 80% confluence in Dulbecco's modified Eagle's medium
620 containing 4.5 g/L glucose and L-glutamine (DMEM, Corning, Corning, NY) supplemented
621 with 10% fetal bovine serum (FBS) and 1% penicillin/streptomycin (Thermo-Fischer) under
622 standard conditions (37 ºC, humidified atmosphere, 5% CO_2). At 80% confluence, cells
623 were trypsinized and replated on CaF_2 coverslips (20 x 20 x 0.35 mm, Crystan, Poole, U.K.)
624 in 35 mm sterile Petri dishes (Corning). Cells were allowed to adhere to the coverslips
625 overnight prior to FA feeding.
626
627 **Palmitic acid labeling**
628 Media was replaced with DMEM containing 4.5 g/L glucose and L-glutamine supplemented
629 with 1% FBS, 1% penicillin/streptomycin and 2-4% of unlabeled or labeled PA conjugated
630 to BSA (final concentrations of palmitic acid between 60-120 μM). Media was not
631 replenished with additional PA at any timepoint.
632

633 **Cell viability assay**
634 Cell viability assays were performed using the Cell Counting Kit-8 assay. Briefly, Huh-7
635 cells were seeded in 96-well plates at a density of 5000 cells per well in 100 µL of DMEM
636 containing 4.5 g/L glucose and L-glutamine supplemented with 10% FBS and 1%
637 penicillin/streptomycin. Cells were cultured in an incubator under standard conditions for
638 24 hours. Media was then removed and replaced with 100 µL of DMEM containing 4.5 g/L
639 glucose and L-glutamine supplemented with 1% FBS, 1% penicillin/streptomycin, and the
640 intended concentration of unlabeled or ^{2}H PA conjugated to BSA or ^{2}H OA conjugated to
641 BSA. Cells were then incubated for the appropriate length of time, either 24, 48, or 72 hours.
642 At each timepoint, 10 µL of CCK-8 solution was added to each well, the plate was incubated
643 for 3 hours, and the absorbance at 450 nm measured.
644
645 **Live cell imaging preparation**
646 At the appropriate times after feeding, cells were rinsed twice with 3 mL of PBS (Corning)
647 and mounted in PBS on a glass microscopy slide (VWR) with a 10 µm double-sided tape
648 spacer (Nitto, San Diego, CA).
649
650 **Fluorescence staining**
651 24 hours after PA feeding, live cells were stained using ER-ID® Red assay kit (GRP
652 CERTIFIED®) (Enzo Life Sciences, Farmingdale, NY) and LipiSpot™ 488 Lipid Droplet
653 Stain (Biotium, Fremont, CA) according to manufacturers' guides. In brief, a staining
654 solution containing 200 µL of 1X assay buffer provided by the ER-ID® Red assay kit, 0.15
655 µL of ER-Red Detection Reagent, 0.15 µL of Hoechst 33342 Nuclear Stain, and 0.2 µL of
656 LipiSpot™ 488 Lipid Droplet Stain was prepared. Cells were rinsed twice with PBS,
657 followed by dispensing the 200 µL of prepared staining solution on the coverslip. Samples
658 were incubated for 30 minutes at 37º C protected from light, after which samples were gently
659 rinsed with 200 µL of 1X assay buffer and mounted on a glass microscopy slide as described
660 above.
661
662 **OPTIR data collection**
663 All imaging was performed as previously described (*11*) on a mIRage-LS IR microscope
664 (Photothermal Spectroscopy Corporation, Santa Barbara, CA) integrated with a four-
665 module-pulsed quantum cascade laser (QCL) system (Daylight Solutions, San Diego, CA)
666 with a tunable range from 932 cm^{-1} to 2348 cm^{-1}. Brightfield optical images were collected
667 using a low magnification 10X refractive objective with a working distance of 15 mm.
668 Spectra and infrared images were collected in co-propagating mode using a 40X
669 Schwarzchild objective with a working distance of 8 mm in transmission mode. Data was
670 collected with an IR laser power of 20 % and a probe power in the range of 11 %. All spectra
671 and images were collected using PTIR Studio 4.6. (Photothermal Spectroscopy
672 Corporation). For hyperspectral images, a step size of 250 nm and one acquisition was used.
673 Spectra were collected using a high signal-to-noise ratio configuration of 200 cm^{-1}/s.
674 Spectra acquisition time was approximately 30 seconds per spectrum. For hyperspectral
675 images, acquisition time was approximately 60 minutes. After hyperspectral imaging, LDs
676 were checked using brightfield or single wavenumber images ensure the cell did not move.
677 If LDs moved during imaging the data was discarded.
678
679 **Fluorescence data collection**
680 Fluorescent images were collected on the mIRage-LS IR microscope using a Prime BSI
681 Express sCMOS (Teledyne, Thousand Oaks, CA). Fluorescent cells were excited using a
682 Sola Light Engine (Lumencor, Beaverton, OR) and a GFP filter cube (TLV-U-FF-GFP,

683 Thorlabs, Newton, NJ), a BFP filter cube (TLV-U-FF-BFP, Thorlabs), or a MCHE filter
684 cube (TLV-U-FF-MCHC, Thorlabs). Images were collected using the 50X objective at 10%
685 LED intensity.
686
687 **FRAP Measurements**
688 FRAP measurements were performed on a Zeiss LSM 880 confocal microscope. Briefly,
689 Huh-7 cells were transfected with ER-mEGFP. ER-mEGFP was a gift from Salvatore
690 Chiantia (Addgene plasmid #182876; http://n2t.net/addgene:182876;
691 RRID:Addgene_182876) (*68*). After 24 hours, media was replaced with DMEM containing
692 4.5 g/L glucose and L-glutamine supplemented with 1% FBS, 1% penicillin/streptomycin
693 and 4% of PA conjugated to BSA or BSA (control). After another 24 hours, cells were
694 fluorescently stained for the ER. FRAP measurements of ER-mEGFP were performed by
695 monitoring the fluorescence of the GFP with 488 nm excitation and 530.5 nm emission.
696 Localization to the ER was confirmed by monitoring the fluorescence of the ER stain with
697 561 nm excitation and 628.5 nm emission. FRAP measurements were taken in the ER of
698 control and ^{2}H PA-fed cells. Initial measurements of the fluorescence intensity were
699 collected with defined Regions of Interest (ROIs) of 7.26 x 7.26 µm for five frames. The
700 GFP was bleached using 488 nm light at a laser power of 100% with a bleach iteration of
701 15 for a total time approximately two seconds. Recovery was monitored for 190 seconds at
702 a scan speed of 1.9 frame per second.
703
704 FRAP curves were normalized to the pre-bleach intensity and baseline corrected by setting
705 the intensity of the first point after bleaching to 0. Curves were then fit to an exponential to
706 determine diffusion time.
707
708 **Data analysis**
709 Fluorescence and brightfield images were processed in Fiji (NIH, Bethesda, MD) (*69*)
710 Spectra were analyzed in IGOR Pro 9 (Wavemetrics, Portland, OR). Live cell ratio images
711 were generated in Python 3.10 in Colab (Google, Mountain View, CA) (*70*) Spectra were
712 background corrected by shifting the baseline towards zero by subtracting by a constant
713 value at 1816 cm^{-1} and then normalized to the 1744 cm^{-1} lipid carbonyl, unless otherwise
714 specified.
715
716 **Lipid droplet ellipticity**
717 Ellipticity was calculated for LDs from cells 27 and 39 hours after being fed 60 µM of ^{2}H
718 PA or ^{2}H OA conjugated to BSA at a 2:1 ratio or control cells at 24 and 48 hours. Ellipticity
719 of LDs was determined in Fiji by measuring the diameter across a LD d_1 and dividing it by
720 the diameter d_2 where d_2 is a 90º angle from d_1. The diameter d_1 was divided by d_2 to obtain
721 an ellipticity for the LD. Ellipticity was calculated for 25 LDs at 27 hours after feeding and
722 25 LDs at 39 hours after feeding for FA fed cells and 25 LDs at 24 hours after feeding and
723 48 hours after feeding for control cells.
724
725 **Limit of Detection**
726 To determine the detection limit of the OPTIR, concentrations of 25 mM, 15 mM, 10 mM,
727 5 mM, 2 mM, and 1 mM of ^{2}H PA dissolved in ethanol and corresponding spectra collected
728 on the OPTIR.
729
730 Detection limit in C=O region. The carbonyl stretch of ^{2}H PA overlaps with the broad C-O
731 stretch of ethanol. To resolve the ^{2}H PA carbonyl stretch, we approximate the C-O stretch
732 of ethanol as linear over the frequency range of the ^{2}H PA carbonyl stretch and draw an

artificial linear baseline below the ^{2}H PA carbonyl stretch (**Fig. S3A-B**). Briefly, the intensities of the raw spectra at two points at either end of the lipid carbonyl, 1744 cm^{-1} and 1680 cm^{-1}, were recorded and fit to a line. The resulting slope intercept formula is used to solve for the baseline intensity at 1708 cm^{-1} (I_B). The baseline intensity at 1708 cm^{-1} was then subtracted from the intensity at 1708 cm^{-1} (I_S) of the raw spectra to obtain a baseline corrected intensity (I_C). These values were then averaged over three spectra per concentration, plotted, and fit to a line to obtain the detection limit for the C=O region (**Fig. S3C**).

Detection limit in C-D region. The ν_{as} CD_2 stretch of ^{2}H PA overlaps slightly with ethanol. To resolve differences in the ν_{as} CD_2 peaks, the baseline was shifted towards zero by subtracting a constant value of the intensity at 2164 cm^{-1} (bringing 2164 cm^{-1} to zero for each spectrum) and then normalized to the ethanol solvent band at 2258 cm^{-1} (**Fig. S3D-E**). The corrected intensities at 2200 cm^{-1} were then averaged over three spectra per ^{2}H PA concentration, plotted, and fit to a line to obtain the detection limit for the C-D region (**Fig. S3F**).

Hyperspectral image analysis

Hyperspectral images were used to determine spatial components of lipid peaks. The second derivative of hyperspectral images were calculated in IGOR Pro 9 to generate single wavenumber images composed of the second derivative of a specified wavenumber. The second derivative of the carbonyl region does not have any contribution from the amide I/water band and the two lipid peaks at 1734 cm^{-1} and 1744 cm^{-1} are separated and can be easily distinguished. Single wavenumber images depicting the intensity of the second derivative of 1744 cm^{-1} and 1734 cm^{-1} were then generated using a code in Python 3.10 in Colab.

Intermediate OPTIR spectra collection

The following intermediates were studied using OPTIR: tripalmitin, 1,2- dipalmitoyl-sn-glycerol, palmitoyl lysophosphatidic acid (Avanti Polar Lipids, Alabaster, AL), 1,2-dipalmitoyl-sn-glycero-3-phosphate (sodium salt) (Avanti Polar Lipids), and palmitic acid. Intermediates were dissolved at 25 mM in dichloromethane (Fisher Scientific) and chloroform.

Lipid extraction and TLC

Cells were cultured in flasks and treated with 60 µM of either BSA, ^{2}H oleic acid, or ^{2}H palmitic acid. At 24 hours after treatment, cells were trypsinized and centrifuged at 3000 *g* for five minutes. The supernatant was discarded, and cells were resuspended in PBS. This process was repeated a second time, where cells were resuspended in 0.8 mL PBS. Lipids were isolated using the Bligh and Dyer method (*71*). In brief, a 3 mL of a cold chloroform/methanol (J.T. Baker, Phillipsburg, NJ) (1:2) solution was added to the resuspended cells, vortexed vigorously and incubated on ice for five minutes. 1 mL of chloroform and 1 mL of PBS was added and the solution vortexed again followed by centrifuging at 1000 *g* for 2 minutes. The bottom layer was recovered by a Pasteur pipette and a second extraction was performed on the cells by adding 1 mL of chloroform and centrifuging again at 1000 *g* for 2 minutes. The bottom layer was recovered again and dried under nitrogen, resuspended in 20 µL chloroform, and spotted on a silica gel plate. Lipids were separated using a mobile phase adapted from Chung *et al* (*72*) of hexane (Thermo Scientific): diethyl ether (Fisher Scientific): acetic acid (J.T. Baker) (80:20:1; v/v/v). TLC plates were then dried for 20 minutes and stained with a 0.2% solution of amido black (Thermo Scientific). The TLC plate was quantified in Fiji by selecting each lane using the

rectangle tool and plotting each lane to visualize the density of each band as a peak and measuring that value.

References

1. S. Iturbe-Rey, C. Maccali, M. Arrese, P. Aspichueta, C. P. Oliveira, R. E. Castro, A. Lapitz, L. Izquierdo-Sanchez, L. Bujanda, M. J. Perugorria, J. M. Banales, P. M. Rodrigues, Lipotoxicity-driven metabolic dysfunction-associated steatotic liver disease (MASLD). *Atherosclerosis* **400**, 119053 (2025).

2. K. Riazi, H. Azhari, J. H. Charette, F. E. Underwood, J. A. King, E. E. Afshar, M. G. Swain, S. E. Congly, G. G. Kaplan, A.-A. Shaheen, The prevalence and incidence of NAFLD worldwide: a systematic review and meta-analysis. *Lancet Gastroenterol Hepatol* **7**, 851–861 (2022).

3. R. T. Brookheart, C. I. Michel, J. E. Schaffer, As A Matter of Fat. *Cell Metab.* **10**, 9–12 (2009).

4. J. A. Olzmann, P. Carvalho, Dynamics and functions of lipid droplets. *Nat Rev Mol Cell Biol* **20**, 137–155 (2019).

5. A. J. Mathiowetz, J. A. Olzmann, Lipid droplets and cellular lipid flux. *Nat Cell Biol* **26**, 331–345 (2024).

6. M. Alves-Bezerra, D. E. Cohen, Triglyceride metabolism in the liver. *Compr Physiol* **8**, 1–8 (2017).

7. B. Bhatt-Wessel, T. W. Jordan, J. H. Miller, L. Peng, Role of DGAT enzymes in triacylglycerol metabolism. *Arch Biochem Biophys* **655**, 1–11 (2018).

8. K. Takeuchi, K. Reue, Biochemistry, physiology, and genetics of GPAT, AGPAT, and lipin enzymes in triglyceride synthesis. *Am J Physiol Endocrinol Metab* **296**, E1195–E1209 (2009).

9. L. Brohée, J. Crémer, A. Colige, C. Deroanne, Lipin-1, a Versatile Regulator of Lipid Homeostasis, Is a Potential Target for Fighting Cancer. *Int J Mol Sci* **22**, 4419 (2021).

10. H. Wang, M. Becuwe, B. E. Housden, C. Chitraju, A. J. Porras, M. M. Graham, X. N. Liu, A. R. Thiam, D. B. Savage, A. K. Agarwal, A. Garg, M.-J. Olarte, Q. Lin, F. Fröhlich, H. K. Hannibal-Bach, S. Upadhyayula, N. Perrimon, T. Kirchhausen, C. S. Ejsing, T. C. Walther, R. V. Farese Jr, Seipin is required for converting nascent to mature lipid droplets. *ELife* **5**, e16582 (2016).

11. H. B. Castillo, S. O. Shuster, L. H. Tarekegn, C. M. Davis, Oleic acid differentially affects lipid droplet storage of de novo synthesized lipids in hepatocytes and adipocytes. *Chem. Commun.* **60**, 3138–3141 (2024).

12. Y. Wei, D. Wang, F. Topczewski, M. J. Pagliassotti, Saturated fatty acids induce endoplasmic reticulum stress and apoptosis independently of ceramide in liver cells. *Am J Physiol Endocrinol Metab* **291**, E275–E281 (2006).

13. M. Ricchi, M. R. Odoardi, L. Carulli, C. Anzivino, S. Ballestri, A. Pinetti, L. I. Fantoni, F. Marra, M. Bertolotti, S. Banni, A. Lonardo, N. Carulli, P. Loria, Differential effect of oleic and palmitic acid on lipid accumulation and apoptosis in cultured hepatocytes. *J. Gastroenterol Hepatol.* **24**, 830–840 (2009).

14. A. Eynaudi, F. Díaz-Castro, J. C. Bórquez, R. Bravo-Sagua, V. Parra, R. Troncoso, Differential Effects of Oleic and Palmitic Acids on Lipid Droplet-Mitochondria Interaction in the Hepatic Cell Line HepG2. *Front Nutr* **8**, 775382 (2021).

15. P. N. Paramitha, R. Zakaria, A. Maryani, Y. Kusaka, B. B. Andriana, K. Hashimoto, H. Nakazawa, S. Kato, H. Sato, Raman Study on Lipid Droplets in Hepatic Cells Co-Cultured with Fatty Acids. *Int J Mol Sci* **22**, 7378 (2021).

16. L. L. Listenberger, X. Han, S. E. Lewis, S. Cases, R. V. Farese, D. S. Ory, J. E. Schaffer, Triglyceride accumulation protects against fatty acid-induced lipotoxicity. *Proc Natl Acad Sci USA* **100**, 3077–3082 (2003).

17. C. Moliterni, F. Vari, E. Schifano, S. Tacconi, E. Stanca, M. Friuli, S. Longo, M. Conte, S. Salvioli, D. Gnocchi, A. Mazzocca, D. Uccelletti, D. Vergara, L. Dini, A. M. Giudetti, Lipotoxicity of palmitic acid is

827 associated with DGAT1 downregulation and abolished by PPARα activation in liver cells. *J Lipid Res* **65**,
828 100692 (2024).

829 18. S. O. Shuster, M. J. Burke, C. M. Davis, Spatiotemporal Heterogeneity of De Novo Lipogenesis in Fixed and
830 Living Single Cells. *J. Phys. Chem. B* **127**, 2918–2926 (2023).

831 19. N. Alsabeeh, B. Chausse, P. A. Kakimoto, A. J. Kowaltowski, O. Shirihai, Cell Culture Models of Fatty Acid
832 Overload: Problems and Solutions. *Biochim Biophys Acta Mol Cell Biol Lipids* **1863**, 143–151 (2018).

833 20. A. M. Kleinfeld, D. Prothro, D. L. Brown, R. C. Davis, G. V. Richieri, A. DeMaria, Increases in serum
834 unbound free fatty acid levels following coronary angioplasty. *Am J Cardiol* **78**, 1350–1354 (1996).

835 21. C. Park, J. M. Lim, S.-C. Hong, M. Cho, Monitoring the synthesis of neutral lipids in lipid droplets of living
836 human cancer cells using two-color infrared photothermal microscopy. *Chem. Sci.* **15**, 1237–1247 (2024).

837 22. M. Portaccio, B. Faramarzi, M. Lepore, Probing Biochemical Differences in Lipid Components of Human
838 Cells by Means of ATR-FTIR Spectroscopy. *Biophysica* **3**, 524–538 (2023).

839 23. X. Chen, K. Chen, J. Hu, Y. Dong, M. Zheng, J. Jiang, Q. Hu, W. Zhang, Palmitic acid induces lipid droplet
840 accumulation and senescence in nucleus pulposus cells via ER-stress pathway. *Commun Biol* **7**, 1–16 (2024).

841 24. M. F. Renne, H. Hariri, Lipid Droplet-Organelle Contact Sites as Hubs for Fatty Acid Metabolism, Trafficking,
842 and Metabolic Channeling. *Front Cell Dev Biol* **9**, 726261 (2021).

843 25. L. Scorrano, M. A. De Matteis, S. Emr, F. Giordano, G. Hajnóczky, B. Kornmann, L. L. Lackner, T. P. Levine,
844 L. Pellegrini, K. Reinisch, R. Rizzuto, T. Simmen, H. Stenmark, C. Ungermann, M. Schuldiner, Coming
845 together to define membrane contact sites. *Nat Commun* **10**, 1287 (2019).

846 26. A. Pérez-Martí, S. Ramakrishnan, J. Li, A. Dugourd, M. R. Molenaar, L. R. De La Motte, K. Grand, A.
847 Mansouri, M. Parisot, S. S. Lienkamp, J. Saez-Rodriguez, M. Simons, Reducing lipid bilayer stress by
848 monounsaturated fatty acids protects renal proximal tubules in diabetes. *ELife* **11**, e74391 (2022).

849 27. M. Piccolis, L. M. Bond, M. Kampmann, P. Pulimeno, C. Chitraju, C. B. K. Jayson, L. P. Vaites, S. Boland, Z.
850 W. Lai, K. R. Gabriel, S. D. Elliott, J. A. Paulo, J. W. Harper, J. S. Weissman, T. C. Walther, R. V. Farese,
851 Probing the Global Cellular Responses to Lipotoxicity Caused by Saturated Fatty Acids. *Mol Cell* **74**, 32-44.e8
852 (2019).

853 28. Adam. Allerhand, P. von R. Schleyer, Solvent Effects in Infrared Spectroscopic Studies of Hydrogen Bonding.
854 *J. Am. Chem. Soc.* **85**, 371–380 (1963).

855 29. K. Pal, I. Samanta, R. K. Gupta, D. Goswami, A. L. Koner, Deciphering micro-polarity inside the endoplasmic
856 reticulum using a two-photon active solvatofluorochromic probe. *Chem. Commun.* **54**, 10590–10593 (2018).

857 30. A. Akoumi, T. Haffar, M. Mousterji, R. S. Kiss, N. Bousette, Palmitate mediated diacylglycerol accumulation
858 causes endoplasmic reticulum stress, Plin2 degradation, and cell death in H9C2 cardiomyoblasts. *Exp Cell Res*
859 **354**, 85–94 (2017).

860 31. F. D. Gunstone, J. L. Harwood, J. L. Harwood, *The Lipid Handbook with CD-ROM* (CRC Press, Boca Raton,
861 FL, ed. 3, 2007).

862 32. G. H. Charbonnet, W. S. Singleton, Thermal properties of fats and oils. *J Am Oil Chem Soc* **24**, 140–142
863 (1947).

864 33. F. O. Cedeño, M. M. Prieto, A. Espina, J. R. García, Measurements of temperature and melting heat of some
865 pure fatty acids and their binary and ternary mixtures by differential scanning calorimetry. *Thermochimica*
866 *Acta* **369**, 39–50 (2001).

867 34. R. N. A. H. Lewis, R. N. McElhaney, Membrane lipid phase transitions and phase organization studied by
868 Fourier transform infrared spectroscopy. *Biochim Biophys Acta* **1828**, 2347–2358 (2013).

869 35. M. Pilarczyk, T. P. Wrobel, M. Baranska, A. Kaczor, Correlation of monomer structures of tripalmitin with the
870 spectroscopic fingerprint of polymorphs: infrared, Raman, and DFT study. *J. Raman Spectrosc* **43**, 1515–1522
871 (2012).

872 36. M. Uematsu, T. Shimizu, Raman microscopy-based quantification of the physical properties of intracellular
873 lipids. *Commun Biol* **4**, 1–15 (2021).

874 37. M. V. Fraile, B. Patrón-Gallardo, G. López-Rodríguez, P. Carmona, FT-IR study of multilamellar lipid
875 dispersions containing cholesteryl linoleate and dipalmitoylphosphatidylcholine. *Chem Phys Lipids* **97**, 119–
876 128 (1999).

877 38. L. Pellegrino, G. Tyagi, E. S. J. Robles, J. T. Cabral, Phase behaviour of model triglyceride ternary blends:
878 triolein, tripalmitin and tristearin. *Phys. Chem. Chem. Phys.* **24**, 29413–29422 (2022).

879 39. T. Sieling, T. Petersen, T. Alpers, J. Christoffers, T. Klüner, I. Brand, CD Stretching Modes are Sensitive to the
880 Microenvironment in Ionic Liquids. *Chemistry* **27**, 17808–17817 (2021).

881 40. E. Tyrode, J. Hedberg, A Comparative Study of the CD and CH Stretching Spectral Regions of Typical
882 Surfactants Systems Using VSFS: Orientation Analysis of the Terminal CH3 and CD3 Groups. *J. Phys. Chem.*
883 *C* **116**, 1080–1091 (2012).

884 41. T. L. Brown, Infrared Intensities And Molecular Structure. *Chem. Rev.* **58**, 581–608 (1958).

885 42. R. Pei, J. Zhang, J. Tan, Y. Luo, S. Ye, Fermi Resonance of the N-D Stretching Mode Probing the Local
886 Hydrogen-Bonding Environment in Proteins. *J. Phys. Chem. B* **128**, 5658–5666 (2024).

887 43. K. Tian, S. Ye, Fermi Resonant Interaction of the Tailed Methyl Groups of Langmuir Monolayer at the
888 Air/Water Interface during Phase Transition. *J. Phys. Chem. C* **119**, 25394–25400 (2015).

889 44. D. J. Moore, M. E. Rerek, Insights into the Molecular Organization of Lipids in the Skin Barrier from Infrared
890 Spectroscopy Studies of Stratum Corneum Lipid Models. *Acta Derm Venereol Suppl* **80**, 16–22 (2000).

891 45. M. F. Renne, R. Ernst, Membrane homeostasis beyond fluidity: control of membrane compressibility. *Trends*
892 *Biochem Sci* **48**, 963–977 (2023).

893 46. Z. Getahun, C.-Y. Huang, T. Wang, B. De León, W. F. DeGrado, F. Gai, Using Nitrile-Derivatized Amino
894 Acids as Infrared Probes of Local Environment. *J. Am. Chem. Soc.* **125**, 405–411 (2003).

895 47. C. G. Bazewicz, M. T. Liskov, K. J. Hines, S. H. Brewer, Sensitive, Site-Specific, and Stable Vibrational Probe
896 of Local Protein Environments: 4-Azidomethyl-l-Phenylalanine. *J. Phys. Chem. B* **117**, 8987–8993 (2013).

897 48. L. Shi, X. Liu, L. Shi, H. T. Stinson, J. Rowlette, L. J. Kahl, C. R. Evans, C. Zheng, L. E. P. Dietrich, W. Min,
898 Mid-infrared metabolic imaging with vibrational probes. *Nat Methods* **17**, 844–851 (2020).

899 49. Y. Bai, C. M. Camargo, S. M. K. Glasauer, R. Gifford, X. Tian, A. P. Longhini, K. S. Kosik, Single-cell
900 mapping of lipid metabolites using an infrared probe in human-derived model systems. *Nat Commun* **15**, 350
901 (2024).

902 50. J. H. Ahn, M. H. Kim, H. J. Kwon, S. Y. Choi, H. Y. Kwon, Protective Effects of Oleic Acid Against Palmitic
903 Acid-Induced Apoptosis in Pancreatic AR42J Cells and Its Mechanisms. *Korean J Physiol Pharmacol* **17**, 43–
904 50 (2013).

905 51. J. A. Ontko, L. W. Perrin, L. S. Horne, Isolation of hepatocellular lipid droplets: the separation of distinct
906 subpopulations. *J Lipid Res* **27**, 1097–1103 (1990).

907 52. J. P. Layerenza, P. González, M. M. García de Bravo, M. P. Polo, M. S. Sisti, A. Ves-Losada, Nuclear lipid
908 droplets: A novel nuclear domain. *Biochim Biophys Acta* **1831**, 327–340 (2013).

909 53. C. Dumesnil, L. Vanharanta, X. Prasanna, M. Omrane, M. Carpentier, A. Bhapkar, G. Enkavi, V. T. Salo, I.
910 Vattulainen, E. Ikonen, A. R. Thiam, Cholesterol esters form supercooled lipid droplets whose nucleation is
911 facilitated by triacylglycerols. *Nat Commun* **14**, 915 (2023).

912 54. M.-C. Popescu, C. Vasile, D. Filip, D. Macocinschi, Gh. Singurel, Characterization by Fourier transform
913 infrared spectroscopy of polyethylene adipate/cholesteryl palmitate blends. *J Appl Polym Sci* **94**, 1156–1163
914 (2004).

915 55. S. Hong, S. Rhee, K. O. Jung, In vivo molecular and single cell imaging. *BMB Rep* **55**, 267–274 (2022).

916 56. X. Li, Y. Li, M. Jiang, W. Wu, S. He, C. Chen, Z. Qin, B. Z. Tang, H. Y. Mak, J. Y. Qu, Quantitative Imaging
917 of Lipid Synthesis and Lipolysis Dynamics in Caenorhabditis elegans by Stimulated Raman Scattering
918 Microscopy. *Anal. Chem.* **91**, 2279–2287 (2019).

919 57. Y. Shen, Z. Zhao, L. Zhang, L. Shi, S. Shahriar, R. B. Chan, G. Di Paolo, W. Min, Metabolic activity induces
920 membrane phase separation in endoplasmic reticulum. *Proc Natl Acad Sci USA* **114**, 13394–13399 (2017).

921 58. J. R. Ferraro, K. Nakamoto, C. Brown, "Basic Theory" in *Introductory Raman Spectroscopy* (Elsevier, ed. 2nd,
922 2003), pp. 1–91.

923 59. X. Teng, T. Xia, J. Yin, M. Li, J. Ao, G. Ding, C. V. Prabhu Dessai, A. M. Isac, D. Matei, H. He, J.-X. Cheng,
924 Mid-Infrared Photothermal Imaging of Fatty Acid Desaturation Reaction in Cancer Cells. bioRxiv [Preprint]
925 (2025). https://doi.org/10.1101/2025.07.02.662881.

926 60. T. O. Eichmann, A. Lass, DAG tales: the multiple faces of diacylglycerol—stereochemistry, metabolism, and
927 signaling. *Cell Mol Life Sci* **72**, 3931–3952 (2015).

928 61. M. C. Petersen, G. I. Shulman, Roles of diacylglycerols and ceramides in hepatic insulin resistance. *Trends*
929 *Pharmacol Sci* **38**, 649–665 (2017).

930 62. K. Lipke, A. Kubis-Kubiak, A. Piwowar, Molecular Mechanism of Lipotoxicity as an Interesting Aspect in the
931 Development of Pathological States—Current View of Knowledge. *Cells* **11**, 844 (2022).

932 63. X. Liu, R. M. Green, Endoplasmic reticulum stress and liver diseases. *Liver Res* **3**, 55–64 (2019).

933 64. F. Sarnyai, A. Somogyi, Z. Gór-Nagy, V. Zámbó, P. Szelényi, J. Mátyási, L. Simon-Szabó, É. Kereszturi, B.
934 Tóth, M. Csala, Effect of cis- and trans-Monounsaturated Fatty Acids on Palmitate Toxicity and on Palmitate-
935 induced Accumulation of Ceramides and Diglycerides. *Int J Mol Sci* **21**, 2626 (2020).

936 65. K. Halbleib, K. Pesek, R. Covino, H. F. Hofbauer, D. Wunnicke, I. Hänelt, G. Hummer, R. Ernst, Activation of
937 the Unfolded Protein Response by Lipid Bilayer Stress. *Mol Cell* **67**, 673-684.e8 (2017).

938 66. F. Wilfling, H. Wang, J. T. Haas, N. Krahmer, T. J. Gould, A. Uchida, J.-X. Cheng, M. Graham, R. Christiano,
939 F. Fröhlich, X. Liu, K. K. Buhman, R. A. Coleman, J. Bewersdorf, R. V. Farese, T. C. Walther, Triacylglycerol
940 Synthesis Enzymes Mediate Lipid Droplet Growth by Relocalizing from the ER to Lipid Droplets. *Dev Cell* **24**,
941 384–399 (2013).

942 67. V. Choudhary, G. Golani, A. S. Joshi, S. Cottier, R. Schneiter, W. A. Prinz, M. M. Kozlov, Architecture of
943 Lipid Droplets in Endoplasmic Reticulum Is Determined by Phospholipid Intrinsic Curvature. *Curr Biol* **28**,
944 915-926.e9 (2018).

945 68. R. A. Petazzi, A. A. Koikkarah, N. D. Tischler, S. Chiantia, Detection of Envelope Glycoprotein Assembly
946 from Old-World Hantaviruses in the Golgi Apparatus of Living Cells. *J Virol* **95**, e01238-20, JVI.01238-20
947 (2021).

948 69. J. Schindelin, I. Arganda-Carreras, E. Frise, V. Kaynig, M. Longair, T. Pietzsch, S. Preibisch, C. Rueden, S.
949 Saalfeld, B. Schmid, J.-Y. Tinevez, D. J. White, V. Hartenstein, K. Eliceiri, P. Tomancak, A. Cardona, Fiji: an
950 open-source platform for biological-image analysis. *Nat Methods* **9**, 676–682 (2012).

951 70. G. Van Rossum, F. L. Drake, *Python 3 Reference Manual* (CreateSpace, Scotts Valley, CA, 2009).

71. T. Okuno, T. Yokomizo, "Basic Techniques for Lipid Extraction from Tissues and Cells" in *Bioactive Lipid Mediators: Current Reviews and Protocols* (Springer Japan, Tokyo, 2015; https://doi.org/10.1007/978-4-431-55669-5_23), pp. 331–336.

72. J. Chung, X. Wu, T. J. Lambert, Z. W. Lai, T. C. Walther, R. V. Farese, LDAF1 and Seipin Form a Lipid Droplet Assembly Complex. *Dev Cell* **51**, 551-563.e7 (2019).

73. S. C. Hsi, A. P. Tulloch, H. H. Mantsch, D. G. Cameron, A vibrational study of the CD2 stretching bands of selectively deuterated palmitic and stearic acids. *Chem Phys Lipids* **31**, 97–103 (1982).

74. A. Filopoulou, S. Vlachou, S. C. Boyatzis, Fatty Acids and Their Metal Salts: A Review of Their Infrared Spectra in Light of Their Presence in Cultural Heritage. *Molecules* **26**, 6005 (2021).

Acknowledgments

We thank Jittima Weerachayaphorn at the Yale Liver Center for the Huh-7 cells and the Ellman group at Yale Chemistry for TLC materials. We thank Joseph S. Wolenski for his assistance in using the Zeiss and Leica confocal microscopes and for his involvement in the design of the FRAP experiments. We also acknowledge use of the Science Hill Light Microscope Facility as these confocal microscopes were essential for our experiments.

Funding:
Anne T. Caldwell Foundation Fund of Coastal Community Foundation
Hevolution/AFAR New Investigator Awardee in Aging and Biology and Geroscience Research (CMD)
Yale Liver Center award National Institute of Health P30 DK034989 (CMD)
National Institute of Health grant T32 GM008283 (HBC)
National Science Foundation Graduate Research Fellowship grant DGE 2139841 (HBC)

Author contributions:

Conceptualization: CMD
Methodology: HBC, CMD
Investigation: HBC, CMD
Visualization: HBC, CMD
Supervision: CMD
Writing—original draft: HBC, CMD
Writing—review & editing: HBC, CMD

Competing interests: The authors declare that they have no competing interests.

Data and materials availability: All data needed to evaluate the conclusions in the paper are present in the paper and/or the Supplementary Materials.